International Journal of Solids and Structures 51 (2014) 945–953

Contents lists available at ScienceDirect

International Journal of Solids and Structures

journal homepage: www.elsevier.com/locate/ijsolstr

Stiffness contribution of cellulose nanofibrils to composite materials

Gabriella Josefsson [a], Fredrik Berthold [b], E. Kristofer Gamstedt [a,*]

[a] Uppsala University, Ångström Laboratory, Department of Engineering Sciences, Box 534, SE-751 21 Uppsala, Sweden
[b] Innventia AB, New Materials & Composites, Box 5604, SE-114 86 Stockholm, Sweden

ARTICLE INFO

Article history:
Received 28 June 2013
Received in revised form 15 November 2013
Available online 27 November 2013

Keywords:
Nanocomposite
Cellulose nanofibrils
Elastic properties
Multiscale modeling
Inverse modeling

ABSTRACT

Nanocomposites, reinforced by different types of cellulose fibrils, have gained increased interest the last years due to the promising mechanical properties. There is a lack of knowledge about the mechanical properties of the cellulose fibrils, and their contribution to the often claimed potential of the impressive mechanical performance of the nanocomposites. This paper investigates the contribution from different types of cellulose nanofibril to the overall elastic properties of composites. A multiscale model is proposed, that allows back-calculation of the elastic properties of the fibril from the macroscopic elastic properties of the composites. The different types of fibrils used were nanofibrillated cellulose from wood, bacterial cellulose nano-whiskers and microcrystalline cellulose. Based on the overall properties of the composite with an unaged polylactide matrix, the effective longitudinal Young's modulus of the fibrils was estimated to 65 GPa for the nanofibrillated cellulose, 61 GPa for the nano whiskers and only 38 GPa for the microcrystalline cellulose. The ranking and absolute values are in accordance with other studies on nanoscale morphology and stiffness estimates. Electron microscopy revealed that in the melt-processed cellulose nanofibril reinforced thermoplastics, the fibrils tended to agglomerate and form micrometer scale platelets, effectively forming a microcomposite and not a nanocomposite. This dispersion effect has to be addressed when developing models describing the structure–property relations for cellulose nanofibril composites.

© 2013 Elsevier Ltd. All rights reserved.

1. Introduction

The majority of composites available today are made of petroleum-based polymers together with synthetic reinforcement fibers, e.g. carbon fiber, aramid fiber or glass fiber. However, the demand of renewable and biodegradable materials is rapidly increasing as the costumers get more aware of the environment. The focus of environmentally friendly composites has led to investigations of alternative constituents for composites. Example of renewable composites could be polylactide (PLA), poly hydroxybutyrate (PHB) or acid cellulose esters reinforced by natural fibers such as wood fibers or flax fibers (Oksman et al., 2003; Wong et al., 2004; Pilla et al., 2009). Such natural cellulose fibers typically have a diameter of 20 μm or more, and a length in the mm range. Prompted by the impressive property improvements of nanosized reinforcement, such as carbon nanotubes (e.g. Thostenson et al. (2001)) and exfoliated nanoclay (e.g. Lau et al. (2006)), there is currently a growing interest in renewable cellulose nanofibre reinforcement in composite materials. In particular for soft polymers matrix materials, e.g. in the rubbery state, considerable stiffness increases can be observed for small amounts of nanosized reinforcement compared with corresponding effects for microscale reinforcements (Papon et al., 2012). With a well-dispersed nanocomposite combining hard fillers and a soft binder, excellent mechanical properties can be achieved, which is also the case for nacre, bone and other biomaterials found in nature (Walther et al., 2010). In comparison to e.g. carbon nanotubes (Dzenis, 2008), cellulose nanofibrils have a functional surface, available for surface modifications to control the fibril–matrix interface and the dispersion of the fibrils in the polymer (Lönnberg et al., 2008). The abundance of hydroxyl groups on the surface cellulose fibrils facilitates interaction with polar matrix systems, and formation of a stiffening network (Rusli and Eichhorn, 2008). Examples of nanoscale cellulose reinforcement are nanofibrillated cellulose (NFC) and bacterial cellulose nano-whiskers (BC) (Siró and Plackett, 2010). Natural cellulose is often present as fibrils (bundles of aligned cellulose molecules) with a width of 10–20 nm and a length of several μm. These fibrils in turn are assembled into larger structures, e.g. plant fibers. By chemomechanical treatment of wood fibers it is possible to liberate the fibrils into so called nanofibrillated cellulose (NFC) (Pääkkö et al., 2007). The terminology for these fibrils with nanoscale lateral dimensions is still not consolidated as pointed out by Chinga-Carrasco (2011). Microfibrillated

* Corresponding author.
E-mail addresses: gabriella.josefsson@angstrom.uu.se (G. Josefsson), fredrik.berthold@innventia.com (F. Berthold), kristofer.gamstedt@angstrom.uu.se (E.K. Gamstedt).

0020-7683/$ - see front matter © 2013 Elsevier Ltd. All rights reserved.
http://dx.doi.org/10.1016/j.ijsolstr.2013.11.018

cellulose (MFC) refers to nanofibrils produced by fibrillation of wood pulp fibers and separation of the cell-wall microfibrils. NFC is used in this work to denote the all types of fibrils made from wood pulp. Another example of nanoscale cellulose reinforcement is bacterial cellulose nano-whiskers (BC) which are produced by a the bacteria *Acetobacter xylimum*, and can be found as one of the constituents in the Asian confectionary *Nata-de-coco* (Budhiono et al., 1999). These nano-whiskers have attracted attention due to its mechanical properties and ability to be used as reinforcement in polymers (Iguchi et al., 2000). Essentially, most research activities have been focused on the important and challenging tasks to manufacture cellulose-based nanocomposites with well-dispersed fibrils. Few studies have investigated the contribution of the potentially stiff nanofibrils to the stiffness of the macroscopic composite material. A deeper understanding of the reinforcing mechanisms could contribute to the development of improved mechanical performance of cellulose nanocomposites. The purpose of the present study is to use a suitable micromechanical model to determine the effective contribution of nanocellulose fibrils to the stiffness of the composite. Composite materials with cellulose contents of 10 wt% have been produced. Three different reinforcing elements were used: microcrystalline cellulose (MCC), bacterial cellulose nano whiskers (BC) or nanofibrillated cellulose (NFC). The fibrils were embedded in a matrix of poly(lactic acid), PLA, a renewable semi-crystalline thermoplastic. Effects of fibril type, degree of crystallinity of the polymer matrix and reinforcement dispersion are discussed.

2. Modelling

A mixed analytical–experimental method is proposed to determine the effective reinforcement stiffness from the composite stiffness. The model includes several parameters, e.g. inclusion shape, inclusion volume fraction, inclusion orientation distribution, elastic properties of the composite and elastic properties of the surrounding matrix and of the inclusions. The structure of the material is based on observed morphologies at high magnification using field-emission scanning electron microscopy. An example is shown in Fig. 1, in addition to micrographs presented in the results section below.

The multiscalar model presented in this paper relates the in-plane isotropic elastic properties of a composite based and the elastic properties of the nanoscale constituents. The model is composed of three dimensional laminate theory (Whitcomb and Noh, 2000), micromechanical model for statistically isotropic composites with arbitrary internal phase geometry by Hashin (1983) and a self-consistent Mori–Tanaka model (Mori and Tanaka, 1973). A schematic illustration of the working process is given in Fig. 2, showing how the elastic properties of the nano and microscale constituents are homogenized to determine the elastic properties of the macroscopic composite.

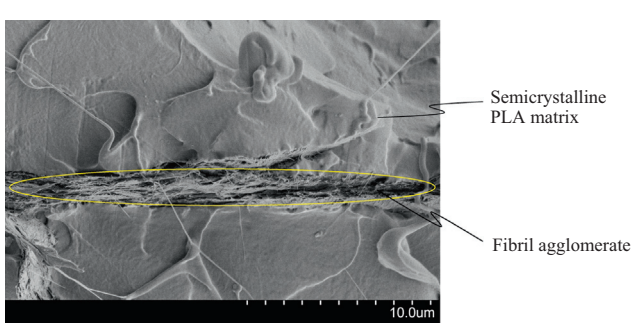

Fig. 1. Cross section of one of the composites reinforced by BC. The image shows a platelet of agglomerated BC imbedded in the matrix.

STEP I. The Young's modulus of a semicrystalline thermoplastic, consisting of crystallites embedded in the matrix in the amorphous state, can be expressed in terms of the elastic properties of the crystalline inclusions (i.e. $E_{m,c}$, $G_{m,c}$, $\nu_{m,c}$), the isotropic constants of the amorphous matrix ($E_{m,a}$, $G_{m,a}$, $\nu_{m,a}$), the volume fraction of the crystallites, $V_{m,c}$, and the volume fraction of the amorphous matrix materials, $V_{m,a}$. Any of the conventional elastic parameters for isotropic materials, i.e. Young's modulus, shear modulus, Poisson ratio and bulk modulus, can be expressed in terms of two other elastic parameters. Here, Hashin's micromechanical model for statistically isotropic composites with arbitrary internal phase geometry was used (Hashin, 1983) to express the properties of the semicrystalline thermoplastic. The model can also be used for particle reinforced composite materials. An exact solution of the moduli for such a material is not available, but relatively close upper and lower bounds for the moduli are given. For the bulk modulus of the semicrystalline matrix, K_m, the bounds are given by

$$K_{m(-)} = K_{m,a} + \frac{V_{m,c}}{\dfrac{1}{K_{m,c} - K_{m,a}} + \dfrac{3V_{m,a}}{3K_{m,a} + 4G_{m,a}}} \tag{1}$$

and

$$K_{m(+)} = K_{m,c} + \frac{V_{m,a}}{\dfrac{1}{K_{m,a} - K_{m,c}} + \dfrac{3V_{m,c}}{3K_{m,c} + 4G_{m,c}}} \tag{2}$$

where $K_{m,c}$ and $K_{m,a}$ are the bulk moduli for the crystalline inclusions and amorphous matrix, respectively. For the shear modulus, the bounds are given by

$$G_{m(-)} = G_{m,a} + \frac{V_{m,c}}{\dfrac{1}{G_{m,c} - G_{m,a}} + \dfrac{6V_{m,a}(K_{m,a} + 2G_{m,a})}{5G_{m,a}(3K_{m,a} + 4G_{m,a})}} \tag{3}$$

$$G_{m(+)} = G_{m,c} + \frac{V_{m,a}}{\dfrac{1}{G_{m,a} - G_{m,c}} + \dfrac{6V_{m,c}(K_{m,c} + 2G_{m,c})}{5G_{m,c}(3K_{m,c} + 4G_{m,c})}} \tag{4}$$

where $G_{m,c}$ and $G_{m,a}$ are the shear moduli for the crystalline inclusions and amorphous matrix, respectively.

By taking the average of the upper and lower bounds of the bulk and shear moduli separately, the elastic parameters of the semicrystalline polymer matrix can be estimated:

$$K_m = \frac{K_{m(-)} + K_{m(+)}}{2} \tag{5}$$

$$G_m = \frac{G_{m(-)} + G_{m(+)}}{2} \tag{6}$$

$$E_m = \frac{9K_m G_m}{3K_m + G_m} \tag{7}$$

When Eqs. (1)–(7) are used for semicrystalline polymers where the inclusions are aggregates of anisotropic crystals, the average isotropic elastic properties of the aggregates have to be determined first. For slow cooling and limited flow during processing, it can be assumed that the crystalline aggregates are effectively isotropic. Although the single crystals are anisotropic, the resulting property of crystalline aggregates is then isotropic, since it is assumed that the crystallites have a random orientation distribution in space. The overall isotropic properties of the crystallite aggregate can be estimated by calculating the Voigt and Reuss shear moduli and bulk moduli. These results are a theoretical upper and lower limit. By taking the average of the Voigt and Reuss moduli, an average isotropic Young's modulus can be estimated (Ravindran et al., 1998). For an orthotropic material the Voigt shear modulus, G_V, and bulk modulus, K_V, are given by

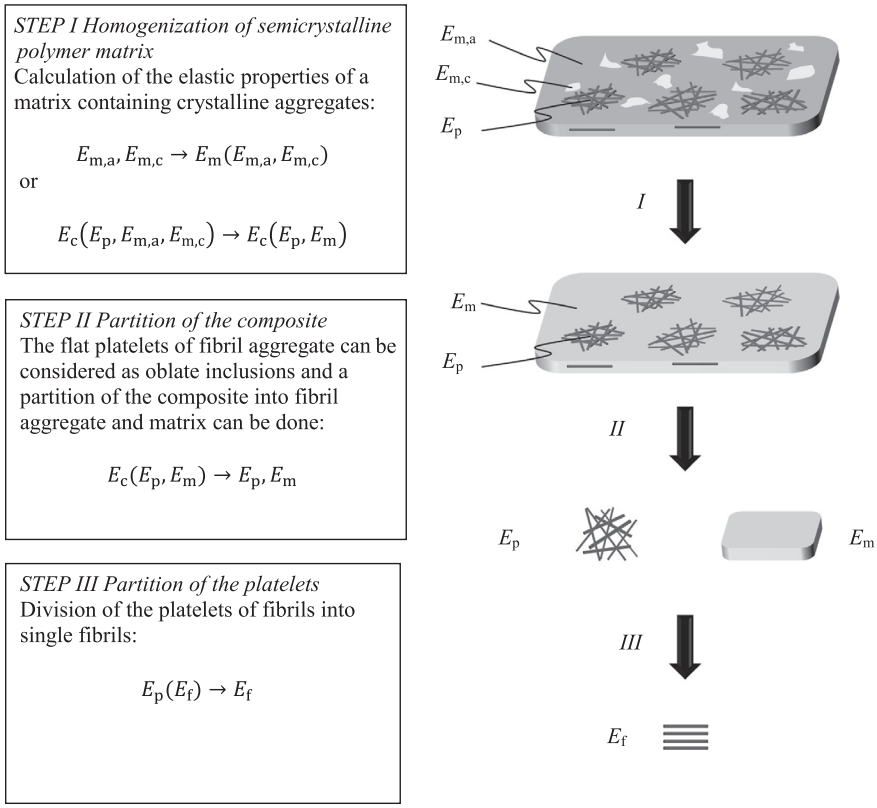

Fig. 2. Schematic illustration of the linked modeling scales, used to relate the stiffness of nanoscale fibrils and that of the macroscopic composite.

$$G_V = \frac{1}{15}(C_{11} + C_{22} + C_{33} - C_{12} - C_{13} - C_{23}) + \frac{1}{5}(C_{44} + C_{55} + C_{66}) \tag{8}$$

and

$$K_V = \frac{1}{9}(C_{11} + C_{22} + C_{33}) + \frac{2}{9}(C_{12} + C_{13} + C_{23}) \tag{9}$$

where C_{ij} are elements in the stiffness matrix of the crystallite.

Corresponding expression for the Reuss shear modulus, G_R, and bulk modulus, K_R, are the following

$$G_R = \frac{15}{4(S_{11} + S_{22} + S_{33}) - 4(S_{12} + S_{13} + S_{23}) + 3(S_{44} + S_{55} + S_{66})} \tag{10}$$

and

$$K_R = \frac{1}{S_{11} + S_{22} + S_{33} + 2(S_{12} + S_{13} + S_{23})} \tag{11}$$

With the averages of the Voigt and Reuss moduli, the effective isotropic Young's modulus of the randomly oriented crystallites to be calculated by

$$E_{m,c} = \frac{9KG}{3K + G} \tag{12}$$

STEP II. A composite reinforced by small platelets of agglomerated fibrils can be considered as a matrix containing aligned and significantly oblate spheroids with the axis of revolution perpendicular to the plane of the composite, as depicted in Fig. 3. The severe oblate shape of the fibril aggregates is most likely a result of the high lateral pressure applied during processing.

Mori–Tanaka effective medium theory can be used to estimate the stiffness for composites reinforced by ellipsoids with aligned axis of revolution, with prolate or oblate shape. The model described below has been reformulated by Benveniste (1987) and define the relation between the overall stiffness of the composite as a function of the elastic properties of the matrix and inclusions. The elastic tensor of the composite can be expressed as

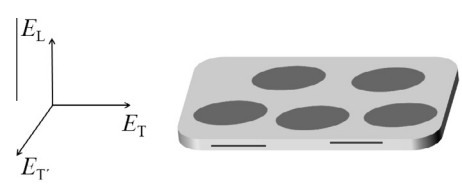

Fig. 3. Schematic image of matrix containing the flat platelets of agglomerated fibrils that can be considered as oblate spheroids lying in the plane of the composite.

$$C_{ij} = C_{ij}^{m} + V^{p}(C_{ik}^{p} - C_{ik}^{m})A_{kj} \tag{13}$$

where C_{ij}^{m} denotes components of the elastic tensor of the matrix material, C_{ik}^{p} are components of the stiffness tensor of the platelets, V^{p} the volume fraction and A_{kj} are components of the strain-concentration tensor. In the Mori–Tanaka model, the strain-concentration tensor can be written

$$A_{ij}^{MT} = A_{ik}^{Esh} N_{kj} \tag{14}$$

where A_{ik}^{Esh} is the inverse of

$$B_{ij} = \delta_{ij} + E_{ik} S_{kl}^{m} \left(C_{lj}^{p} - C_{lj}^{m} \right) \tag{15}$$

and N_{kj} is the inverse of

$$M_{ij} = (1 - V^{p})\delta_{ij} + V^{p} A_{ij}^{Esh} \tag{16}$$

The symbol δ_{ij} denotes components of the identity tensor, S_{ij}^{m} are components of the compliance tensor for the isotropic amorphous

cellulose, and E_{ik} are components of the Eshelby tensor (Eshelby, 1957). The Eshelby tensor for a transversely isotropic inclusion in an isotropic matrix depends only on inclusion aspect ratio and the elastic constants of the matrix. For better accuracy, the model can be further used in a self-consistent scheme, where the strain-concentration tensor and the Eshelby tensor then becomes a function of the composite properties. Such a procedure is described by Josefsson et al. (2013). With assumptions on the ratios between the elastic parameters of the inclusions, the self-consistent scheme can be used to iteratively back-calculate the stiffness of the inclusion.

STEP III. The stiffness of a platelet consisting of agglomerated fibril can be determined from the stiffness of the single fibrils by using 3D laminate theory. A 3D laminate theory has been presented by Whitcomb and Noh (2000), and used by Joffre et al. (2013) in integral form for composites with an in-plane fiber orientation distribution. Here, the expressions are simplified, in closed analytical form, for composites with an in-plane random fiber orientation, or more precisely for platelets with an in-plane random nanofibril orientation. The interaction induced by the fibril–fibril bonds is not described by assuming fused joints as in a truss network, but rather through the assumption of uniform strain through the thickness of the envisaged laminate structure. This assumption is generally made for dense fiber networks, such as well-consolidated paper (e.g. Salmén et al. (1984)). Furthermore, some assumptions of the fibril shape and elastic properties have to be made. High-resolution SEM images showed that the fibrils can be described as reasonably straight rods, and the waviness or curl the fibrils is neglected. The straight fibrils are assumed to extend from one side of the platelets to the other. They are also assumed to be transversely isotropic, with the main axis in the 1-direction. The simplified expressions of the components of the elastic tensor of the platelet, C^{p}_{ij}, expressed in terms of the components of the elastic tensor of the fibril material, C^{f}_{ij}, are:

$$C^{p}_{11} = C^{p}_{22} = \frac{3}{8}C^{f}_{11} + \frac{1}{4}C^{f}_{12} + \frac{3}{8}C^{f}_{22} + \frac{1}{2}C^{f}_{66} - \frac{1}{8}\frac{\left(C^{f}_{12} - C^{f}_{23}\right)^{2}}{C^{f}_{33}} \tag{17}$$

$$C^{p}_{12} = \frac{1}{8}C^{f}_{11} + \frac{3}{4}C^{f}_{12} + \frac{1}{8}C^{f}_{22} - \frac{1}{2}C^{f}_{66} + \frac{1}{8}\frac{\left(C^{f}_{12} - C^{f}_{23}\right)^{2}}{C^{f}_{33}} \tag{18}$$

$$C^{p}_{33} = C^{f}_{33} \tag{19}$$

$$C^{p}_{13} = C^{p}_{23} = \frac{1}{2}C^{f}_{13} + \frac{1}{2}C^{f}_{23} \tag{20}$$

$$C^{p}_{44} = C^{p}_{55} = \frac{2C^{f}_{44}C^{f}_{55}}{C^{f}_{44} + C^{f}_{55}} \tag{21}$$

$$C^{p}_{66} = \frac{C^{p}_{11} - C^{p}_{12}}{2} \tag{22}$$

With these expressions, the contributing fibril stiffness can be identified from the platelet stiffness.

3. Experimental procedures

3.1. Materials

Nanofibrillated cellulose (NFC) was prepared from commercially available bleached sulphite pulp (Super aceta, Borregaard), as described by Pääkkö et al. (2007). The bleached fibers are first enzymatically treated to loosen the cell wall and thereafter passed through a high-pressure fluidizer (Microfluidizer M-110EH, Microfluidics Corp., USA) in order to liberate the NFC. The consistency of the NFC slurry was in this study about 2–3 wt%. As has been described elsewhere (e.g. Pääkkö et al., 2007), the typical diameter of the produced NFC will be between 5 and 30 nm and the length above 1 μm. The microcrystalline cellulose (MCC) used was purchased from Aldrich (product code: 310697), and has an average size 20 μm. Before use the MCC was swelled in water over night. Bacterial cellulose (BC) was extracted from Nata-de-Coco (Chef's choice food manufacture, Thailand) essentially according to the recipe of Lee et al. (2011). In this work, 300 g (dry weight) of BC was washed three times with 3 l de-ionized water. Washed BC was thereafter levigated using a laboratory shredder (Waring LB20EG) followed by treatment with a homogenizer (Polytron PT 10–35 GT). Excess water was removed using centrifugation (11000*g* for 15 min). Thereafter the slurry was treated four times with 1 M NaOH at 80 °C for 20 min. After washing to a neutral pH, a 2.5 l cellulose slurry with a consistency of 0.6% was obtained. Before manufacturing the composite, the slurry was further homogenized using a Microfluidizer processor M110 EH (Microfluidics) with 2 passes through 400 μm + 200 μm followed by one pass through 200 μm + 100 μm. The size of BC fibrils extracted from Nata-de-Coco is typically about 50 nm in width and several μm in length, as has been quantified by Lee et al. (2011).

The PLA used in this study was grade 8052D (NatureWorks LLC). The D isomer content of this quality is stated to be from 3.7 to 4. PLA granules were further ground into particles (ICO Polymers, USA) with a size between 15 and 150 μm.

3.2. Composite preparation

The composites were produced using a two-step procedure; in the first step PLA and cellulose were pre-formed into a puck-shaped cake, utilizing a wet casting technique that, in the second step, was compression moulded at slightly above the PLA melting point to form the final composite sample. The pre-formed cakes were prepared from accurately weighed cellulose and PLA mixed together in deionized water to achieve a well-dispersed slurry. The NFC and BC containing slurries was prepared by directly adding PLA powder to the measured amount of NFC/BC suspension needed to prepare the pre-formed cake. The PLA was added under vigorous mixing. The volume of the PLA containing mixture was then adjusted to 300 ml by adding dH_2O under stirring. After the volume adjustment the slurry was sonicated for three minutes and thereafter poured into a straight wall glass funnel (Ø 50 mm), where the bottom of the funnel was covered with a Millipore Durapore filter (catalogue number 04700, 0.65 μm DVPP filter). At the bottom outlet, vacuum was applied to remove water. As water drained from the funnel, more of the slurry was added until the full 300 ml had been transferred to the funnel. For slurries containing MCC, a measured amount of cellulose was transferred to 300 ml dH_2O under sonication to achieve a fine dispersion. The PLA was carefully added to the MCC solution and sonication continued for 5 min after which the slurry was poured into the funnel. In all preparations of the pre-formed cakes, the vacuum was removed when the water level sank to the top of the solid sediment, after which the samples were carefully moved onto a blotting paper. The samples were thereafter dried in a vacuum oven at 40 °C overnight followed by drying at 65 °C the following night in the same oven. The composition of produced pre-formed cakes was 10 wt% cellulose and 90 wt% PLA. The target weight of a cake was 4.75 g. After drying, the samples were placed inside a 2.0 mm thick metal frame. The frame had six holes with a diameter of 52 mm each, ensuring that the samples fit well. The frame was placed between 1 cm thick steel plates. A covering Teflon film was placed between the plates and the frame. The assembly was placed in a heated pressing tool and pressed for 20 min using a dial

pressure of 150 bars and a temperature of 185 °C. The chosen temperature is well above the melting point of the used PLA, T_m = 158 °C. Nakagaito et al. (2009) showed that the storage modulus of composites with high fibril content was not significantly affected by increased temperature up to 250 °C, which indicates that the fibrils do not degrade at the used temperature. Unlike injection moulding and extrusion, there was no appreciable flow in the mould. The disks could then be assumed to be in-plane isotropic, which was later qualitatively corroborated by microstructural analysis using scanning electron microscopy.

After pressing the samples were rapidly cooled under maintained pressure using water. To study the effect of matrix crystallinity, half of the composite samples were annealed (aged) after hot pressing (65 °C, 2–3 h) by heat treatment in an oven at 95 °C for 20 min.

The produced disks had a diameter of 52 mm and from each disk three dog-bone specimens were cut using water jet. The samples were conditioned in a climate chamber at 23 °C and 55% relative humidity for more than 24 h to assure that equilibrium was reached before mechanical testing.

3.3. Mechanical testing

Mechanical tests were performed with a tensile machine, Shimadzu AGS-X. A video extensometer, TRViewX Shimadzu, was connected to the tensile machine, which optically measured the axial strain in the gauge section of the samples. The distance between the end clamps was 26 mm and the gauge length of the extensometer was 16 mm. The tensile tests were carried until ultimate failure with a stroke rate of 1 mm/minute, which corresponds to a strain rate of $6.4 \times 10^{-4}\ s^{-1}$. The Young's modulus was determined at the initial slope of the linear part of the stress–strain curve. At this stage, the deformation was linear with no sign of damage formation or any other inelastic behavior.

3.4. Degree of crystallinity

A double cycle differential scanning calorimetry (DSC), DSC Q1000 from TA instruments, was performed with a speed of 1 °C/min from 20 to 200 °C.

3.5. Scanning electron microscope

To investigate the dispersion and orientation of the reinforcing fibrils, scanning electron microscopy was performed. The images were taken with a cold field emission scanning electron microscope, Hitachi S-4800, at an accelerating voltage of 0.7 kV. The samples were not coated or altered before imaging.

4. Results and discussion

4.1. Inverse modeling of the elastic properties of the fibrils

From the elastic properties of the macroscopic composites, the elastic properties of the nanoscale fibrils were estimated with the described model. The input data used were the in-plane isotropic Young's modulus of the composite, the isotropic Young's modulus of the PLA matrix, volume fraction and some assumption of the degree of anisotropy of the reinforcing fibrils.

As a consequence of the aging, PLA becomes partly crystalline (Lim et al., 2008). It is well known that the crystallinity of the PLA affects the elastic properties of the PLA, and thereby the elastic properties of the composite (Harris and Lee, 2008). As the crystalline phase of PLA is much stiffer than the amorphous PLA, the stiffness of the PLA will increase when the degree of crystallinity increases. In order to not overestimate the stiffness of the fibrils from the back-calculation it is essential to take into account the increase in stiffness of the PLA by the increase of crystallinity. The crystalline content of the PLA was measured by DSC from the first cycle of the thermal sweep. The degree of crystallinity of the composites was then determined by

$$\chi = \frac{\Delta H_m - \Delta H_c}{H_m^c w} \tag{23}$$

where ΔH_m is the enthalpy of fusion, ΔH_c is the enthalpy of crystallization, H_m^c is the enthalpy of fusion of a PLA crystal of infinite size, and w is the weight fraction of PLA. Here, $H_m^c = 93$ J/g has been used (Tsuji and Ikada, 1995; Lim et al., 2008).

The crystallinity obtained from the DSC measurement is the weight fraction of crystal, but with the assumption of a similar density of the amorphous and crystalline phases the weight fraction and volume fraction are effectively the same. With the obtained degree of crystallinity, the Young's modulus of the PLA matrix can be calculated as described in *STEP I* for each annealed sample by using the Hashin model for materials containing particles, or crystals, with irregular shape, i.e. Eqs. (1)–(7). The crystallinity is then used as volume fraction of inclusions in the model. Young's modulus for the amorphous PLA is taken from the tensile test of pure amorphous PLA and the Poisson ratio, ν, is taken to be 0.35 (Baiardo et al., 2004; Wright-Charlesworth et al., 2005). The properties of the crystalline PLA is taken from Lin et al. (2010) where the stiffness tensor for different types of crystalline PLA is presented. Here it is assumed that the PLA crystals are in the most stable stereocomplex (sc) form, and the elastic tensor is given by

$$(C_{ij})^{sc-form} = \begin{pmatrix} 16.75 & 6.69 & 10.50 & 0.13 & 0 & 0 \\ 6.69 & 16.75 & 10.50 & -0.13 & 0 & 0 \\ 10.50 & 10.50 & 24.67 & 0 & 0 & 0 \\ 0.13 & -0.13 & 0 & 0.82 & 0 & 0 \\ 0 & 0 & 0 & 0 & 0.82 & 0.13 \\ 0 & 0 & 0 & 0 & 0.13 & 5.03 \end{pmatrix} [\text{GPa}]$$

With this elastic tensor and the experimentally characterized properties of the semi-crystalline PLA, the Young's moduli of the various PLA matrix materials were calculated and summarized in Table 1. For the non-aged sample, the PLA was in the amorphous state and an average Young's modulus of 3.80 GPa was determined from 6 tensile tests of pure PLA. Surprisingly, the estimated Young's modulus of the PLA matrix is higher than that of the MCC-reinforced PLA.

With the calculated elastic properties of the matrix, the contribution to the elastic properties of the composites from fibril platelets can be identified by inverse solving of the self-consistent scheme. The composite stiffness is a function of the stiffness properties of the constituents and the volume fraction of fibril aggregates and of the matrix. The volume fraction can be defined by the weight fraction of the fibrils, W_f, the density of the fibrils, ρ_f, and the density of the composite, ρ_c, by

Table 1
The average Young's moduli of the annealed composites and the estimated Young's moduli of the corresponding PLA matrices.

Reinforcement	Composite Young's modulus [GPa]	PLA degree of crystallinity [%]	PLA matrix Young's modulus [GPa]
10 wt% MCC (aged)	4.30	40.4	4.88
10 wt% BC (aged)	4.63	30.9	4.60
10 wt% NFC (aged)	4.69	32.6	4.65

$$V_f = W_f \frac{\rho_c}{\rho_f} \tag{24}$$

where

$$\rho_c = V_f \rho_f + V_m \rho_m = V_f \rho_f + (1 - V_f)\rho_m \tag{25}$$

By solving this equation for V_f, the volume fraction is determined. From pycnometric measurements, the density of the PLA was found to be 1.26 g/m^3. It was assumed that the density of crystalline PLA is not much higher than that of amorphous PLA. Both phase densities were therefore set to 1.26 g/m^3. The density of the cellulose fibrils was taken to be 1.50 g/m^3 (Eichhorn et al., 2010; Decoux et al., 2004).

4.2. Microcrystalline cellulose

MCC consists of highly crystalline cellulose. It is produced from wood pulp by acid hydrolysis to remove the amorphous cellulose, and the polycrystalline aggregates are assumed to have arbitrary geometry with statistically isotropic properties and an aspect ratio of ~1 (Mathew et al., 2005). SEM images were taken at the fracture surfaces of the composites, where well-defined MCC particles clearly presented themselves. Fig. 4 shows a MCC particle with a diameter in the 10–20 μm range.

MCC particles are built of aggregates of single cellulose crystallites, where the crystals are orthotropic. For calculation of elastic properties of composites reinforced by crystalline aggregates, the mean isotropic properties of the aggregates have to be estimated. That could be done by using the average of the Voigt and Reuss assumptions, i.e. Eqs. (8)–(12). The mean isotropic properties of the aggregates can then be inserted in Eqs. (1)–(7), and together with the elastic properties of the matrix, the elastic properties of the composite become a function of the elastic properties of the MCC particles. For inverse solution of Eqs. (1)–(7), some assumptions of the elastic properties are required. Here, a fixed ratio between all elastic moduli of the crystallites and the Young's modulus in the main axis, E_3, of the crystal was assumed. With more than one fitting parameter, the estimation of these parameters becomes very sensitive and far from robust. The Young's modulus in the main axis of the crystallites is the stiffness parameter that typically has the largest impact on the composite stiffness. The elastic tensor calculated by Eichhorn and Davies (2006) for crystalline cellulose I_β, determined from the crystal structure evaluated by Nishiyama et al. (2002), was used with the modification that the C_{56} and C_{65} components were ignored, in order to make the material orthotropic. The anisotropy ratios were chosen to be same as for the orthotropic version of Eichhorn and Davies elastic tensor for crystalline cellulose. The Young's modulus of the PLA matrix was taken from the tensile test of pure PLA. The crystallinity was measured by DSC, and as described in *STEP I*, the corresponding Young's modulus of the semi-crystalline PLA matrix was defined. With the measured Young's modulus of the composite, and the elastic properties of the PLA, Eqs. (1)–(7) were solved with respect to the Young's modulus of the single crystallites in the main axial direction. The results are presented in Table 2. The randomly oriented polycrystalline MCC particles have an isotropic Young's modulus of a modest 7.8 GPa. For the aged PLA, the Young's modulus of the predicted semicrystalline matrix was even higher than of the measured value of the composite. This led to unrealistically low stiffness values of the reinforcement.

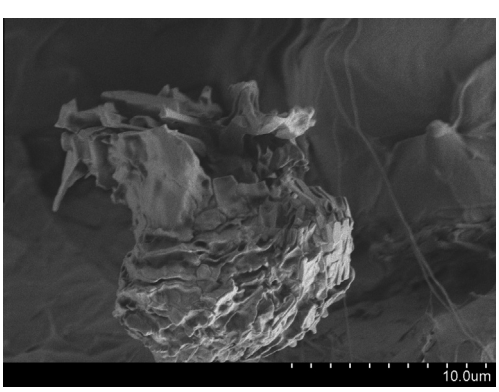

Fig. 4. MCC particle at a composite fracture surface. The MCC particles have an aspect ratio of ~1 and a diameter of around 10–20 μm.

Table 2
Young's moduli of MCC reinforced composites and its constituents.

Young's modulus [GPa]				
Sample	Composites	PLA	MCC crystal (main axis)	MCC aggregate (isotropic)
10 wt% MCC	4.05	3.8	38.3	7.81
10 wt% MCC (aged)	4.30	4.88	–	–

4.3. Nanofibrillated cellulose

NFC are fibrils with high aspect ratio, e.g. Henriksson et al. (2007). Due to the abundance of hydroxyl groups and relatively poor fibril-matrix compatibility, the fibrils tend to agglomerate. SEM images showed that the fibrils formed platelets oriented in the plane of the composite, see Fig. 5.

From image analysis of the SEM images, the aspect ratio of the fibril platelets could be determined. The protruding aggregates and pits from pulled-out aggregates indicate that the aggregates along the fracture surface of the composite did not fracture, but remained unbroken and essentially intact. Many of the visible aggregates were protruding approximately by the same amount as the observed aggregate radius, which indicates that fracture plane coincides with the mid-plane of the aggregate. In this case, the aspect ratio of the aggregates can be estimated by direct measurements in the SEM images. By measuring the thickness and diameter of the platelets in the fracture plane of the composite, the aspect ratio of the NFC platelets can be determined. Measurement was done on 5 platelets and the average aspect ratio was estimated to $\alpha = 0.15$. In the micromechanical model, the platelets were considered as aligned oblate spheroids with the axis perpendicular to the composite as in the schematic image shown in Fig. 3.

Some assumptions regarding the relations between the elastic parameters of the fibrils have to be done in the inverse model. Here, ratios between the longitudinal Young's modulus of the fibrils, $E_{f,L}$, and all other elastic moduli were fixed. The predicted composite stiffness then becomes a function of only one variable, i.e. $E_{f,L}$. The anisotropy ratios are based on micromechanical modeling of single NFC fibrils characterized by high-resolution transmission electron microscopy (Josefsson et al., 2013):

$$\frac{E_{f,T}}{E_{f,L}} = 0.36 \tag{26}$$

$$\frac{G_{f,LT}}{E_{f,L}} = 0.055 \tag{27}$$

$$\frac{G_{f,T}}{E_{f,L}} = 0.14 \tag{28}$$

The Poisson ratios used were computed by the model presented by Josefsson et al. (2013): $\nu_{f,LT} = 0.24$, $\nu_{f,TL} = 0.09$ and $\nu_{f,TT} = 0.32$. The layered structure observed inside the NFC platelets suggests

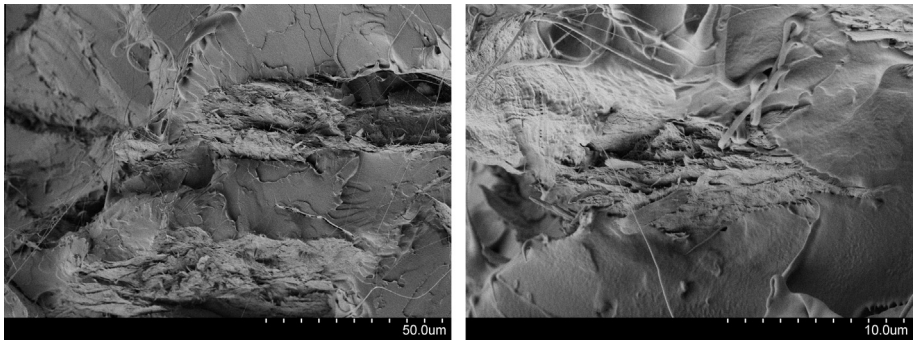

Fig. 5. The NFC fibrils agglomerated during the processing, and formed platelets embedded in the PLA matrix. The SEM images show the fracture cross section from a tensile test where the platelets of fibrils are clearly displayed, as well as PLA fibrils from crazes formed during the fracture process (Liu et al., 2012).

Table 3
Sample and constituent average elastic properties of the NFC composites.

Young's modulus [GPa]			
Sample	Composites	PLA	NFC
10 wt% NFC	5.00	3.80	65.1
10 wt% NFC (aged)	4.69	4.65	10.5

that laminate theory can describe the in-plane stiffness. Although not of the same importance as the in-plane stiffness, the out-of-plane stiffness plays a role and is needed as input in the Mori–Tanaka model, described in *STEP II*. A three-dimensional laminate model, as described in *STEP III*, is therefore justified (e.g. Whitcomb and Noh (2000)). With the above anisotropy ratios and the three-dimensional laminate theory, i.e. Eqs. (17)–(22), the platelet stiffness becomes a function of the sought longitudinal Young's modulus of the fibril. The next step is to insert the platelet stiffness values in the self-consistent Mori–Tanaka model described in Eqs. (13)–(16). The overall elastic properties of the composite then become a function of the longitudinal Young's modulus of the fibril. The contributing fibril stiffness is thus identified from the measured Young's modulus of the composite. The results are presented in Table 3. The contributing longitudinal Young's modulus of the NFC was estimated to 65 GPa from the unaged sample. The corresponding value for the aged samples with partially crystalline PLA matrix was only 10 GPa, which is significantly lower other reported values (Josefsson et al., 2013).

4.4. Bacterial cellulose whiskers

The composites made of BC had similar stiffness properties as the composites made of NFC (cf. Table 1). As NFC, BC fibrils have very high aspect ratios (Moon et al., 2011). During the preparation of the composites, the BC fibrils agglomerated and formed platelets that lie in the plane of the composite disks, as shown in Fig. 6. The thickness of the platelets is significantly smaller than for NFC composites, which suggests that BC are more easily dispersed in PLA than NFC. Tomé et al. (2011) noticed that a PLA-matrix composite becomes more transparent with BC reinforcement, than with NFC reinforcement. This is a clear sign of a finer dispersion for the BC composite as compared with the NFC composite. By direct observation in SEM, 5 measurements of the aspect ratio of typical BC platelets were made, and the average aspect ratio was estimated to $\alpha = 0.02$. The inverse modeling of the elastic properties of BC was done in the same manner as for NFC outlined above, and the results are presented in Table 4. The effective longitudinal Young's modulus of the BC fibrils was estimated to be 61 GPa for the unaged composite. Again, the fibril stiffness for the aged material was significantly lower than expected, indicating that the PLA stiffness predictions might not be adequate.

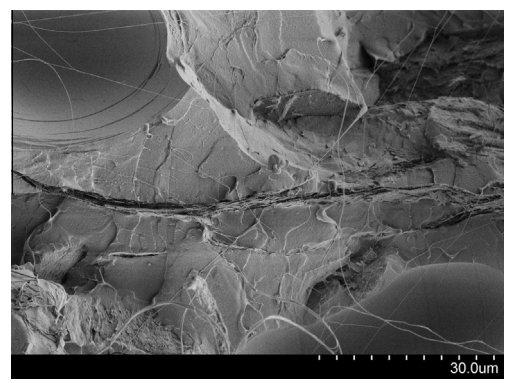

Fig. 6. The BC fibrils tend to agglomerate during melt processing and form platelets embedded in the PLA matrix, as seen as a horizontal layer in the middle of the SEM image. The individual fibrils crossing the micrograph in other directions are PLA craze fibrils and not BC fibrils.

Table 4
Sample and constituent average elastic properties of the BC composites.

Young's modulus [GPa]			
Sample	Composites	PLA	BC
10 wt% BC	5.78	3.80	61.4
10 wt% BC (aged)	4.63	4.60	10.1

4.5. Comparisons

The back-calculated values of the fibril stiffness from the aged composite samples were consistently lower than expected; 10 GPa for NFC and BC, and indeterminate for MCC. The unaged composite samples have a purely amorphous PLA matrix from rapid cooling after hot-press moulding. The stiffness of the quenched amorphous PLA has been experimentally characterized, whereas the stiffness of the semi-crystalline aged PLA is predicted by homogenization described in *STEP I*, Eqs. (1)–(12). Since cellulose fibrils are not expected to degrade at 95 °C for a short period of time, the unrealistically low values of effective fibril stiffness are most likely due to an overestimation of the stiffness of the semi-crystalline PLA matrix. In the presence of even small amounts of moisture, the degradation rate of PLA can be considerable even at moderately elevated temperatures (Reed and Gilding, 1981), as under the present heat treatment conditions.

The Young's modulus of the fibrils estimated from the micromechanical model and the properties of the unaged composite samples showed reasonable agreement with values found in

Table 5
Young's modulus of NFC estimated in this work together with values found in the literature.

Material	Young's modulus	Method	Ref.
NFC	65	Back-calculation	This work
NFC	61–107	AFM bending	Cheng et al. (2009)
NFC	29–36	Raman spectroscopy, back-calculation	Tanpichai et al. (2012)

Table 6
Young's modulus of BC estimated in this work together with values found in the literature.

Material	Young's modulus	Method	Ref.
BC	61	Back-calculation	This work
BC	78 ± 17	AFM	Guhados et al. (2005)
BC	79–88	Raman spectroscopy, back-calculation	Tanpichai et al. (2012)

literature. A value of 38 GPa for the Young's modulus was lower than expected. However, Eichhorn and Young (2001) performed Raman spectroscopy on MCC and together with back-calculation a value of the Young's modulus of 25 GPa was found. A possible reason for these relatively low stiffness values is that the low aspect ratio of MCC, which can reduce the stress transfer ability between load carrying reinforcement. Debonding and damage accumulation is not accounted for the models used to determine the contributing stiffness. In Tables 5 and 6, the Young's modulus for NFC and BC, respectively, are compared with values found in literature. The variability is large, but the back-calculated values are comparable to the cited experimental results.

A common trait of all the investigated cellulose nanofibril composites is that the nanoscale reinforcing units formed plate-like or particulate aggregates in the microscale, i.e. the material is not a well-dispersed nanocomposite. Hence, the nanocomposite effect of significantly improved mechanical properties substantially beyond rule-of-mixtures predictions can be ruled out in the effective microcomposites in this work. A contributing mechanisms to the nanocomposite effect is that the polymer mobility is reduced in the close vicinity of stiff reinforcements, which manifests itself in increases in the glass-transition temperature and local stiffness on the nanometer scale (Papon et al., 2012). A viable path to improve dispersion of cellulose nanofibrils in PLA, and other thermoplastics suitable for melt processing, is surface treatment of the fibrils for improved compatibility with the matrix (Lee et al., 2009; Tomé et al., 2011). Despite using a fine powder instead of conventional polymer pellets, the dispersion remained relatively poor for the presently studied composites, with fibril agglomerates on the micrometer scale. The benefits of the large specific surface area of the nanofibrils on local polymer matrix immobilization is there not expected (Kalfus and Jancar, 2007). A micromechanical model for stiffness predictions of nanocomposites necessarily needs to account for the immobilization effect, e.g. by a stiffness enhancement factor for the intragallery modulus in clay nanocomposites introduce by Luo and Daniel (2003). Such an approach was however not necessary here, since the agglomerates were fairly large and the specific surface area of the reinforcing elements relatively low.

5. Conclusions

Direct measurements of cellulose nanofibril stiffness are not practical for engineering purposes. The main purpose of these fibrils in composites is to convey improved mechanical properties, such as stiffness. An indirect way to assess the reinforcement efficiency of the cellulose fibrils is to use inverse modeling to estimate the contributing fibril stiffness to that of the composite. The axial Young's modulus of fibrils was determined to be 65 GPa for nanofibrillated cellulose and 61 GPa for bacterial cellulose, which is in concert with stiffness estimates elsewhere. The effective Young's modulus along the main axis of the crystal entities in microcrystalline cellulose was estimated to be 38 GPa. The developed model gives reasonable results for high-aspect ratio fibrils and for composites with well-defined matrix properties. The presented model accounts for fibril agglomerates, which is an unwanted yet common feature for melt processed cellulose nanofibril reinforced thermoplastics.

Acknowledgments

The authors wish to thank Julia Netrval at Spectral Solutions AB for able help with the electron microscopy.

References

Baiardo, M., Zini, E., Scandola, M., 2004. Flax fibre–polyester composites. Compos. A 35 (6), 703–710.
Benveniste, Y., 1987. A new approach to the application of Mori–Tanaka's theory in composite materials. Mech. Mater. 6 (2), 147–157.
Budhiono, A., Rosidi, B., Taher, H., Iguchi, M., 1999. Kinetic aspects of bacterial cellulose formation in nata-de-coco culture system. Carbohydr. Polym. 40 (2), 137–143.
Cheng, Q., Wang, S., Harper, D.P., 2009. Effects of process and source on elastic modulus of single cellulose fibrils evaluated by atomic force microscopy. Compos. A 40 (5), 583–588.
Chinga-Carrasco, G., 2011. Cellulose fibres, nanofibrils and microfibrils: The morphological sequence of MFC components from a plant physiology and fibre technology point of view. Nanoscale Res. Lett. 6 (1), 1–7.
Decoux, V., Varcin, É., Leban, J.-M., 2004. Relationships between the intra-ring wood density assessed by X-ray densitometry and optical anatomical measurements in conifers. Consequences for the cell wall apparent density determination. Ann. Forest Sci. 61 (3), 251–262.
Dzenis, Y.A., 2008. Structural nanocomposites. Science 319, 419–420.
Eichhorn, S.J., Davies, G.R., 2006. Modelling the crystalline deformation of native and regenerated cellulose. Cellulose 13 (3), 291–307.
Eichhorn, S.J., Young, R.J., 2001. The Young's modulus of a microcrystalline cellulose. Cellulose 8 (3), 197–207.
Eichhorn, S.J., Dufresne, A., Aranguren, M., Marcovich, N.E., Capadona, J.R., Rowan, S.J., Weder, C., Thielemans, W., Roman, M., Renneckar, S., Gindl, W., Veigel, S., Keckes, J., Yano, H., Abe, K., Nogi, M., Nakagaito, A.N., Mangalam, A., Simonsen, J., Benight, A.S., Bismarck, A., Berglund, L.A., Peijs, T., 2010. Review: current international research into cellulose nanofibres and nanocomposites. J. Mater. Sci. 45 (1), 1–33.
Eshelby, J.D., 1957. The determination of the elastic field of an ellipsoidal inclusion, and related problems. Proc. R. Soc. Lond. A 241 (1226), 376–396.
Guhados, G., Wan, W., Hutter, J.L., 2005. Measurement of the elastic modulus of single bacterial cellulose fibers using atomic force microscopy. Langmuir 21 (14), 6642–6646.
Harris, A.M., Lee, E.C., 2008. Improving mechanical performance of injection molded PLA by controlling crystallinity. J. Appl. Polym. Sci. 107 (4), 2246–2255.
Hashin, Z., 1983. Analysis of composite materials. J. Appl. Mech. 50 (2), 481–505.
Henriksson, M., Henriksson, G., Berglund, L.A., Lindström, T., 2007. An environmentally friendly method for enzyme-assisted preparation of microfibrillated cellulose (MFC) nanofibers. Eur. Polymer J. 43 (8), 3434–3441.
Iguchi, M., Yamanaka, S., Budhiono, A., 2000. Bacterial cellulose – a masterpiece of nature's arts. J. Mater. Sci. 35 (2), 261–270.
Joffre, T., Wernersson, E.L.G., Miettinen, A., Luengo Hendriks, C.L., Gamstedt, E.K., 2013. Swelling of cellulose fibres in composite materials: constraint effects of the surrounding matrix. Compos. Sci. Technol. 74, 52–59.
Josefsson, G., Tanem, B., Li, Y., Vullum, P., Gamstedt, E.K., 2013. Prediction of elastic properties of nanofibrillated cellulose from micromechanical modeling and nano-structure characterization by transmission electron microscopy. Cellulose 20 (2), 761–770.
Kalfus, J., Jancar, J., 2007. Immobilization of polyvinylacetate macromolecules on hydroxyapatite nanoparticles. Polymer 48 (14), 3935–3937.
Lau, K.-T., Gu, C., Hui, D., 2006. A critical review on nanotube and nanotube/nanoclay related polymer composite materials. Compos. Part B 37 (6), 425–436.
Lee, K.-Y., Blaker, J.J., Bismarck, A., 2009. Surface functionalisation of bacterial cellulose as the route to produce green polylactide nanocomposites with improved properties. Compos. Sci. Technol. 69 (15), 2724–2733.
Lee, K.-Y., Quero, F., Blaker, J., Hill, C.S., Eichhorn, S., Bismarck, A., 2011. Surface only modification of bacterial cellulose nanofibres with organic acids. Cellulose 18 (3), 595–605.

Lim, L.T., Auras, R., Rubino, M., 2008. Processing technologies for poly(lactic acid). Prog. Polym. Sci. 33 (8), 820–852.
Lin, T., Liu, X.-Y., He, C., 2010. Ab initio elasticity of poly(lactic acid) crystals. J. Phys. Chem. B 114 (9), 3133–3139.
Liu, H., Chen, N., Fujinami, S., Louzguine-Luzgin, D., Nakajima, K., Nishi, T., 2012. Quantitative nanomechanical investigation on deformation of poly(lactic acid). Macromolecules 45 (21), 8770–8779.
Lönnberg, H., Fogelström, L., Berglund, L., Malmström, E., Hult, A., 2008. Surface grafting of microfibrillated cellulose with poly(ε-caprolactone) – synthesis and characterization. Eur. Polym. J. 44 (9), 2991–2997.
Luo, J.-J., Daniel, I.M., 2003. Characterization and modeling of mechanical behavior of polymer/clay nanocomposites. Compos. Sci. Technol. 63 (11), 1607–1616.
Mathew, A.P., Oksman, K., Sain, M., 2005. Mechanical properties of biodegradable composites from poly lactic acid (PLA) and microcrystalline cellulose (MCC). J. Appl. Polym. Sci. 97 (5), 2014–2025.
Moon, R.J., Martini, A., Nairn, J., Simonsen, J., Youngblood, J., 2011. Cellulose nanomaterials review: structure, properties and nanocomposites. Chem. Soc. Rev. 40 (7), 3941–3994.
Mori, T., Tanaka, K., 1973. Average stress in matrix and average elastic energy of materials with misfitting inclusions. Acta Metall. 21 (5), 571–574.
Nakagaito, A.N., Fujimura, A., Sakai, T., Hama, Y., Yano, H., 2009. Production of microfibrillated cellulose (MFC)-reinforced polylactic acid (PLA) nanocomposites from sheets obtained by a papermaking-like process. Compos. Sci. Technol. 69 (7–8), 1293–1297.
Nishiyama, Y., Langan, P., Chanzy, H., 2002. Crystal structure and hydrogen-bonding system in cellulose Iβ from synchrotron X-ray and neutron fiber diffraction. J. Am. Chem. Soc. 124 (31), 9074–9082.
Oksman, K., Skrifvars, M., Selin, J.F., 2003. Natural fibres as reinforcement in polylactic acid (PLA) composites. Compos. Sci. Technol. 63 (9), 1317–1324.
Pääkkö, M., Ankerfors, M., Kosonen, H., Nykänen, A., Ahola, S., Österberg, M., Ruokolainen, J., Laine, J., Larsson, P.T., Ikkala, O., Lindström, T., 2007. Enzymatic hydrolysis combined with mechanical shearing and high-pressure homogenization for nanoscale cellulose fibrils and strong gels. Biomacromolecules 8 (6), 1934–1941.
Papon, A., Montes, H., Hanafi, M., Lequeux, F., Guy, L., Saalwächter, K., 2012. Glass-transition temperature gradient in nanocomposites: evidence from nuclear magnetic resonance and differential scanning calorimetry. Phys. Rev. Lett. 108 (6), 065702.
Pilla, S., Gong, S., O'Neill, E., Yang, L., Rowell, R.M., 2009. Polylactide-recycled wood fiber composites. J. Appl. Polym. Sci. 111 (1), 37–47.
Ravindran, P., Fast, L., Korzhavyi, P.A., Johansson, B., Wills, J., Eriksson, O., 1998. Density functional theory for calculation of elastic properties of orthorhombic crystals: application to TiSi2. J. Appl. Phys. 84 (9), 4891–4904.
Reed, A.M., Gilding, D.K., 1981. Biodegradable polymers for use in surgery – poly(glycolic)/poly(lactic acid) homo and copolymers: 2. In vitro degradation. Polymer 22 (4), 494–498.
Rusli, R., Eichhorn, S.J., 2008. Determination of the stiffness of cellulose nanowhiskers and the fiber–matrix interface in a nanocomposite using Raman spectroscopy. Appl. Phys. Lett. 93, 033111.
Salmén, L., Carlsson, L., Ruvo, A.D., Fellers, C., Htun, M., 1984. A treatise on the elastic and hygroexpansional properties of paper by a composite laminate approach. Fibre Sci. Technol 20 (4), 283–296.
Siró, I., Plackett, D., 2010. Microfibrillated cellulose and new nanocomposite materials: a review. Cellulose 17 (3), 459–494.
Tanpichai, S., Quero, F., Nogi, M., Yano, H., Young, R.J., Lindström, T., Sampson, W.W., Eichhorn, S.J., 2012. Effective young's modulus of bacterial and microfibrillated cellulose fibrils in fibrous networks. Biomacromolecules 13 (5), 1340–1349.
Thostenson, E.T., Ren, Z., Chou, T.-W., 2001. Advances in the science and technology of carbon nanotubes and their composites: a review. Compos. Sci. Technol. 61 (13), 1899–1912.
Tomé, L.C., Pinto, R.J., Trovatti, E., Freire, C.S., Silvestre, A.J., Neto, C.P., Gandini, A., 2011. Transparent bionanocomposites with improved properties prepared from acetylated bacterial cellulose and poly (lactic acid) through a simple approach. Green Chem. 13 (2), 419–427.
Tsuji, H., Ikada, Y., 1995. Properties and morphologies of poly(l-lactide): 1. Annealing condition effects on properties and morphologies of poly(l-lactide). Polymer 36 (14), 2709–2716.
Walther, A., Bjurhager, I., Malho, J.-M., Pere, J., Ruokolainen, J., Berglund, L.A., Ikkala, O., 2010. Large-area, lightweight and thick biomimetic composites with superior material properties via fast, economic, and green pathways. Nano Lett. 10 (8), 2742–2748.
Whitcomb, J., Noh, J., 2000. Concise derivation of formulas for 3D sublaminate homogenization. J. Compos. Mater. 34 (6), 522–535.
Wong, S., Shanks, R., Hodzic, A., 2004. Interfacial improvements in poly(3-hydroxybutyrate)-flax fibre composites with hydrogen bonding additives. Compos. Sci. Technol. 64 (9), 1321–1330.
Wright-Charlesworth, D.D., Miller, D.M., Miskioglu, I., King, J.A., 2005. Nanoindentation of injection molded PLA and self-reinforced composite PLA after in vitro conditioning for three months. J. Biomed. Mater. Res., Part A 74A (3), 388–396.